

Electronic Level Structure and Single Electron Tunneling Effects in CdSe Quantum Rods

ELI ROTHENBERG,^a TALEB MOKARI,^a MIRI KAZES,^a URI BANIN,^{a,*} DAVID KATZ,^b DOV STEINER,^b AND ODED MILLO^{b,*}
^aInstitute of Chemistry and the Center for Nanoscience and Nanotechnology; ^bRacah Institute of Physics and the Center for Nanoscience and Nanotechnology, The Hebrew University of Jerusalem, Jerusalem 91904, Israel

(Received 20 May 2003)

Abstract. Optical spectroscopy and scanning tunneling microscopy are used to study the size and shape dependence of the electronic states in CdSe quantum rods. Samples having average rod dimensions ranging from 10 to 60 nm in length and 3.5 to 7 nm in diameter, with aspect ratios varying between 3 to 12, were investigated. Both size-selective optical spectroscopy and tunneling spectra on single rods show that the level structure depends primarily on the rod diameter and not on length. With increasing diameter, the band gap and the excited state level spacings shift to the red. The level structure is assigned using a multi-band effective-mass model. We shall also discuss the effect of single electron charging on the tunneling spectra, possibly reflecting the quantum rod level degeneracy, and its dependence on the tunneling junction parameters.

INTRODUCTION

Colloidal semiconductor nanocrystals are a class of nanomaterials that manifest the transition from the molecular limit to the bulk solid-state regime,¹⁻³ with significant potential for serving as building blocks of nano-devices in applications ranging from lasers^{4,5} and opto-electronic devices⁶ to biological fluorescence tagging.⁷ Shape control of such colloidally prepared nanostructures has been recently achieved by modifying the synthesis to obtain rod-shaped particles—quantum rods (QRs).^{8,9} QRs exhibit electronic and optical properties that differ from quantum dots (QDs). For example, unlike the spherical dots, QRs have linearly polarized emission as demonstrated by fluorescence measurements on single rods,^{10,11} leading also to polarized lasing.⁵ In our recent work¹² we combined optical and tunneling spectroscopies on CdSe QRs and correlated the experimental data with the level structure calculated using a multi-band effective-mass model for an infinite potential well.

In this paper we present further studies of the electronic level structure of CdSe QRs, and its dependence on rod length and diameter, by correlating tunneling and

optical spectroscopic data with calculations performed for a finite potential-well model. Additionally, tunneling experiments and simulations investigating single-electron charging phenomena were performed in order to resolve the degeneracy of different QR energy levels, as done previously for QDs.^{2,13} Our study provides significant insight into the evolution of the electronic structure from zero-dimensional QDs to one-dimensional quantum wires.

The combination of scanning-tunneling and optical spectroscopies has proven to be a powerful approach to decipher the level structure of spherical nanocrystal QDs.^{2,14} While in the optical spectra, allowed valence band (VB) to conduction band (CB) transitions are detected,^{15,16} in tunneling spectroscopy the CB and VB states can be probed separately, yielding complementary information on the level structure.^{2,13,17-19} Such data can provide an important benchmark for theoretical models of the level structure in strongly quantum-confined nanostructures, as was demonstrated for spherical QDs.²⁰⁻²² Multi-band effective-mass approaches,^{15,16,23}

*Authors to whom correspondence should be addressed.
E-mails: banin@chem.ch.huji.ac.il; milode@vms.huji.ac.il

atomistic pseudo-potential theory,²⁰ and semi-empirical tight binding modeling^{21,22} were used to describe measured QD size-dependent level spectra. Recently, both multi-band effective-mass theory²⁴ and the pseudo-potential approach^{25,26} were applied for calculating the size-dependent energy levels in QRs.

EXPERIMENTAL

CdSe QRs were grown using the well-developed methods of colloidal nanocrystal synthesis, where the rods are overcoated by organic ligands, as reported in detail elsewhere.^{8,27–29} Two methods were used to prepare CdSe rods. Briefly, 4 g of TOPO (trioctylphosphineoxide) and 0.32 g (20% by mole) of HPA (hexyl phosphonic acid) or 0.52 g (20% by mole) of TDPA (tetradecyl phosphonic acid) were heated in a three-neck flask on a Schlenk line under Ar atmosphere to a temperature of 360 °C with vigorous stirring.

Method A utilizes a stock solution containing both Cd and Se with the amounts being 0.164 g Cd(CH₃)₂ (1.15 mmole) and 0.09 g Se (1.15 mmole) dissolved in 2.8 g TBP (16.4 mmole) or TOP, yielding a Cd:Se ratio of 1:1. Here 2 g of cold stock solution was rapidly injected and the solution was cooled to 290 °C. Further growth begins two minutes after the first injection, by drop-wise addition of the required amount (depending on the required size) of CdSe stock solution at an approximate rate of 0.25 mL/min, followed by half an hour of annealing.

In method B for synthesizing CdSe rods, separate stock solutions are used for Cd and Se. For rod nucleation, Cd(CH₃)₂ and Se were dissolved in TBP in separate flasks, where the Cd solution was 0.162 g (1.13 mmole) of Cd(CH₃)₂ in 0.34 g TBP (2 mmole), and the Se solution—0.064 g of Se (0.81 mmole) dissolved in 1.45 g of TBP (8.5 mmole). For rod growth, 0.03 g of Cd(Me)₂ (0.21 mmole) was dissolved in 0.12 g of TBP (0.7 mmole) and Se solution—0.0168 g Se (0.21 mmole) in 0.13 g of TBP (0.76 mmole). All solutions were kept in a refrigerator at –30 °C. Utilizing two-stock solutions, the Cd stock solution was added drop-wise at 360 °C and one minute later the Se stock solution was injected rapidly and the solution was cooled to 290 °C. Twenty minutes after the Se injection, rods can be grown further by adding the Cd growth solution followed by addition of the Se growth solution 2 min later (the molar ratio Cd:Se is 1:1), repeating such injections for achieving the required length after a waiting time of 40 min. The reaction was stopped half an hour after the last injection. The growth was monitored by measuring the absorption spectra of aliquots extracted from the reaction solution. Upon reaching the desired size, the reaction mixture was allowed to cool down to room temperature.

The size distribution of the rods was determined from transmission electron microscope (TEM) images by measuring at least 200 particles and fitting the length and diameter histograms to a Gaussian distribution. In a typical reaction the size distribution was on the order of ±10% for the diameters and ±15% for the lengths. Figure 1 presents four different QR

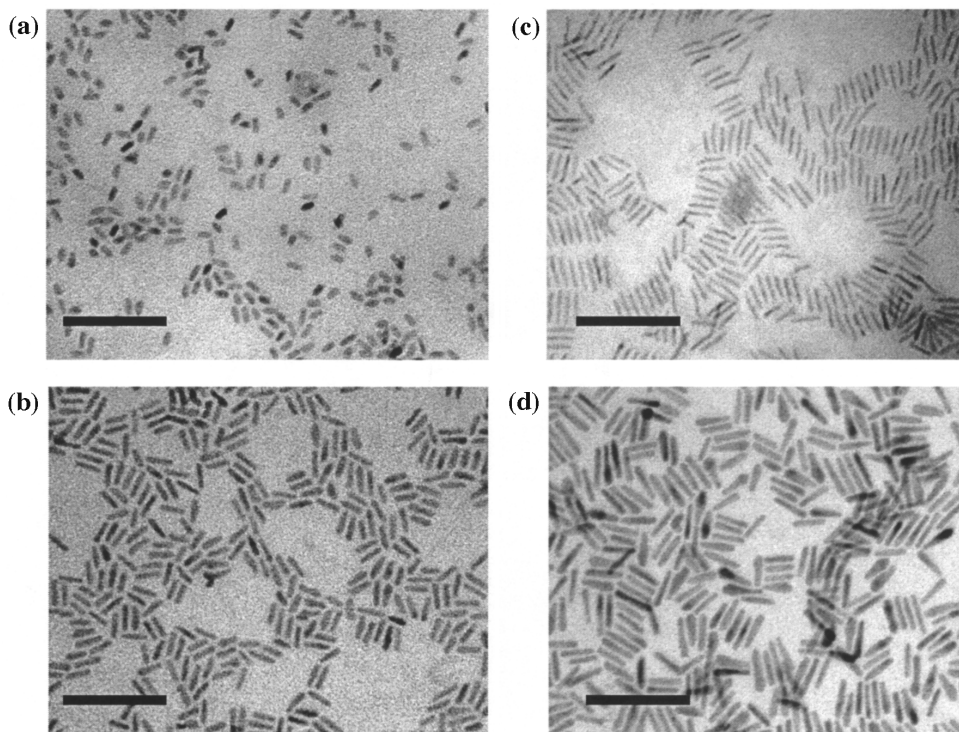


Fig. 1. TEM images of four CdSe QR samples with average length × diameter, (a) 11 × 5.5 nm, (b) 20 × 4.5 nm, (c) 29 × 3.7 nm, (d) 33 × 6.5 nm. Scale bar is 100 nm.

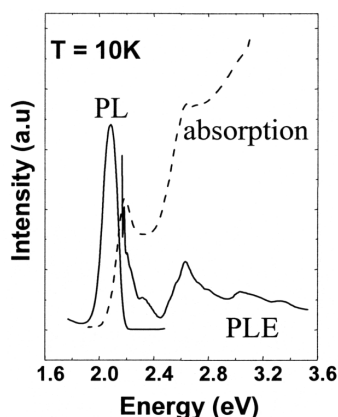


Fig. 2. Optical spectroscopy methods applied to the QRs. Absorption, emission (PL), and size-selective PLE spectra of a 21×3.7 nm (on average) QR sample.

samples, manifesting the good control over the QRs dimensions and size distribution.

Low temperature ($T = 10$ K) optical spectroscopy measurements were performed on QRs embedded in a free-standing polymer film. The samples exhibited absorption spectra with several transitions and a distinct photoluminescence (PL) peak, assigned to band-gap emission, as shown in Fig. 2. These spectra suffer, however, from inhomogeneous broadening. Improved size-selectivity and spectral resolution were achieved by applying photoluminescence excitation (PLE) spectroscopy that probes the size-dependent absorption level structure of the nanocrystals. Here, one measures the excitation spectra using a narrow detection window on the blue side of the inhomogeneously broadened PL peak. The detection window selects a subset of the inhomogeneous sample, and structured excitation spectra showing transitions from VB to CB states in QRs of a specific size are obtained. The measurements were carried out on different QR samples, where the rod diameter and length were varied systematically, and a few detection energies, E_{det} , were used for each sample.

For the scanning tunneling microscopy (STM) measurements, the QRs were deposited on a conducting substrate applying two different methods, resulting in two distinct sample configurations. The tunneling spectra (dI/dV versus V characteristics) were obtained using the double barrier tunnel junction (DBTJ) configuration, by positioning the tip above a *single* QR. In the first deposition method, which is illustrated in Fig. 3a, the QRs were spin-coated on highly oriented pyrolytic graphite (HOPG) substrate from a highly diluted QRs-hexane (or toluene) solution to obtain a “QR/HOPG configuration”. The tip was retracted far away from the QR, thus suppressing single-electron charging effects.^{13,19} In addition, CB (VB) states appear at positive (negative) sample bias and the peak separations are close to the real QR level spacing. The second method is presented in Fig. 3b, in which the QRs were anchored to atomically smooth gold surface via hexanedithiol (DT) molecules, yielding the “QR/DT/Au configuration”. These DT molecules increase the QR–substrate distance, and the tunneling rate in this junction typically becomes slower in comparison to the tip–QR junction. Consequently, single-electron charging effects become significant,^{2,3} as opposed to what is typically observed for the QR/HOPG system. Moreover, the peak separations were often much larger than the real QR level spacing, due to the effect of voltage division between the two tunneling junction.^{13,18,19} In both methods, as shown theoretically for QDs, the applied voltage does not much affect the level spectrum.^{21,22} Hence, the dI/dV versus V spectra yield direct information on the QR level structure and single-electron charging effects.^{13,18,19}

RESULTS

In order to study the length and diameter dependence of the level structure, various QR samples were investigated having average dimensions ranging from 3.5 to 7 nm in diameter (d) and from 10 to 60 nm in length. The optical spectra (at 10 K) show that the positions of the absorption onset and PL peak red-shifted with increasing diameter and showed no significant variation with rod length.³¹ The PLE spectra presented in Fig. 4 are less

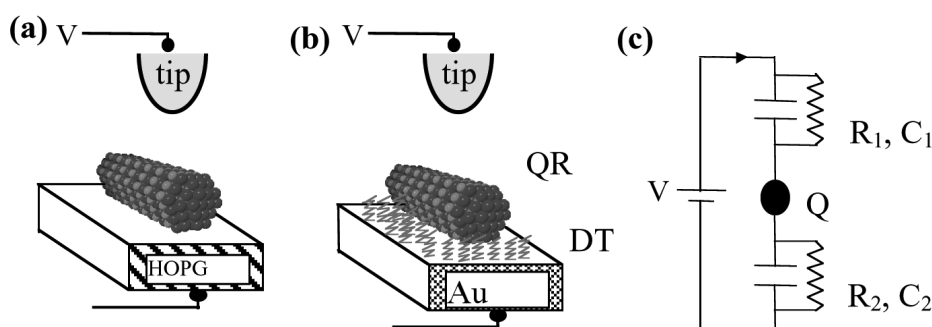


Fig. 3. Schematic of the DBTJ configurations used for acquiring the tunneling spectra. The QR in (a) is directly deposited on HOPG, while that in (b) is anchored to a gold substrate via DT molecules. The equivalent circuit is shown in (c).

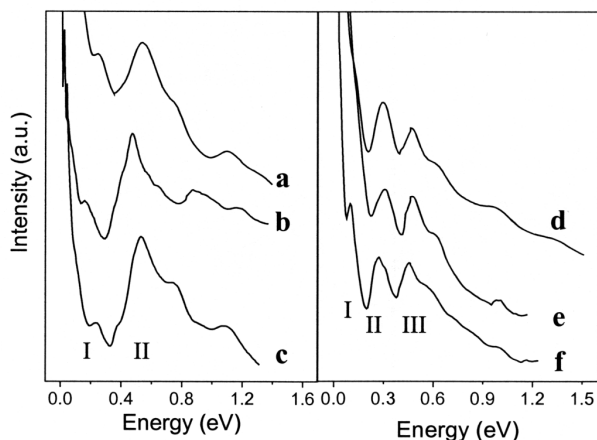


Fig. 4. PLE spectra obtained at 10 K for six CdSe QR samples: (a) 31×3.8 nm (length \times diameter on average), $E_{\text{det}} = 2.25$ eV; (b) 21×3.7 nm, $E_{\text{det}} = 2.16$ eV; (c) 11×3.2 nm, $E_{\text{det}} = 2.25$ eV; (d) 60×6.7 nm, $E_{\text{det}} = 2.00$ eV; (e) 30×6.5 nm, $E_{\text{det}} = 2.01$ eV; (f) 11×5.8 nm, $E_{\text{det}} = 2.03$ eV, with the zero energy representing the position of the detection window, E_{det} . Relevant optical transitions are denoted as I, II, and III. The structure above 0.7 eV results from overlapping peaks of the excitation lamp that could not be completely normalized out.

structured as compared with those measured on QDs¹⁵ due to the increased sources of inhomogeneous broadening in rods and due to the intrinsically less discrete level structure. A striking feature is the nearly identical level structure observed for the three QR samples of small diameter (traces a, b, and c), which differs significantly from the spectra measured on the thicker rods (traces d, e, and f), although in each group the aspect ratio varies from 3 to about 10. This shows clearly that not only the band-gap of the rods depends mainly on the diameter, but also the excited optical transitions. This property demonstrates the quasi one-dimensionality of the QRs in the range studied here, in the sense that the QR length is larger than the bulk exciton Bohr radius in CdSe (5.7 nm), while the diameter is smaller. Thus, strong confinement pertains for the radial direction only, while weak confinement is approached for the axial direction.

We now turn to describe our single QR tunneling spectra. Figure 5 presents STM images of QRs on a gold substrate. These substrates were smooth at the atomic level, thus enabling one to clearly identify the adsorbed rods. The gold surface exhibited large terraces, atomic-height steps, and dislocations running along the $\langle 110 \rangle$ directions, typical of (111)-oriented gold films. The images in Fig. 5 were acquired at room temperature, where the tip-sample drift was too large for reliable measure-

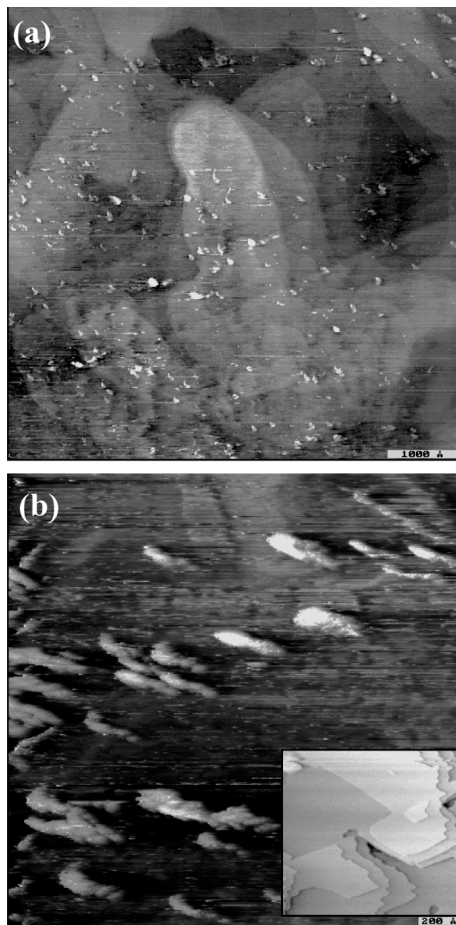


Fig. 5. (a) 0.6×0.6 mm² STM image of a CdSe-QR\DT\Au sample at room temperature. Image (b), 200×200 nm², exhibits the rod shape of the QRs, with sizes around 30×5 nm. The surface morphology of the bare gold film is presented in the inset (300×280 nm²), in which atomic steps and dislocations typical of Au(111) surfaces are seen.

ments of local single-rod I-V tunneling spectra. Only at cryogenic temperatures STM spectroscopy of isolated CdSe QRs, on both gold and HOPG, was realized. Figure 6 presents STM images of QRs deposited on HOPG substrates (measured at 4.2 K). Single QRs were observed (Fig. 6a) as well as clusters of QRs (Fig. 6b) showing their tendency to aggregate on the HOPG surface.

Tunneling spectra measured on the QRs further demonstrate that the QR level structure depends primarily on the diameter of the QRs, not on their length, in accordance with the PLE data. This behavior is depicted in Fig. 7, showing tunneling spectra at 4.2 K for QRs deposited on HOPG of different diameters and lengths. Most significantly, the region of suppressed tunneling

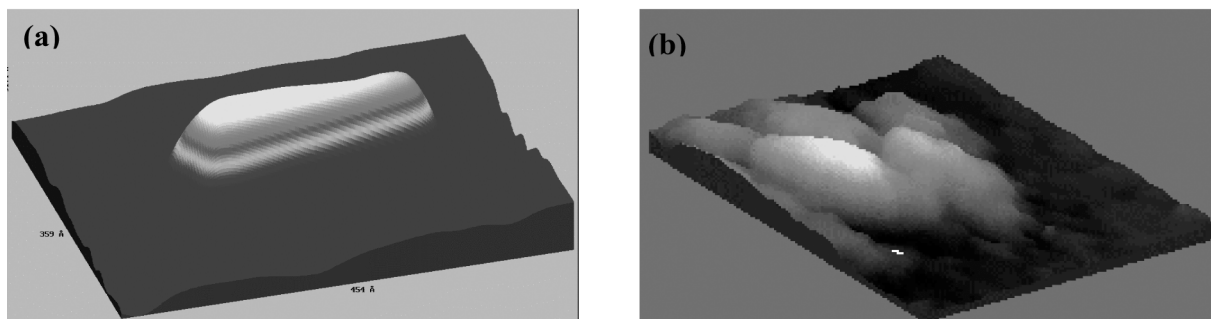


Fig. 6. STM topographic images of (a) a single CdSe QR 25 nm long and 4 nm in diameter, and (b) QRs aggregate, deposited on HOPG.

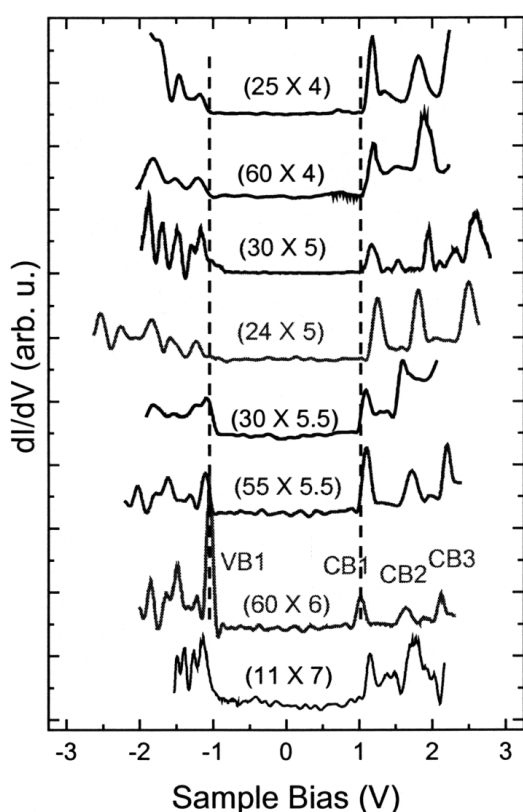


Fig. 7. dI/dV versus V tunneling spectra at 4.2 K for CdSe QRs deposited on HOPG. QRs dimensions (length \times diameter) are marked above each curve in nm. For clarity, the spectra were shifted horizontally to position the band gap symmetrically relative to zero bias. The tunneling set values were in the range $V_s = 1.5 - 2$ V and $I_s = 50 - 80$ pA. CB1, CB2, and CB3 at positive bias, and VB1 at negative bias denote the main peaks of the spectra that are addressed in the text. The vertical dashed lines are guides to the eye in order to demonstrate the blue shift of the band gap with decreasing QR diameter.

conductance (null density of states) around zero bias, associated with the quasi-particle energy gap, is red-shifted upon QR thickening from about 2.4 eV in the upper two curves ($d = 4$ nm and two significantly different lengths) to about 2.1 eV in the curve second from the bottom ($d = 6$ nm). This trend was not observed as clearly for the spacing between the CB ground state (CB1) and the first excited state (CB2). Level CB3 was observed in about 50% of the measured rods, where the current did not reach the saturation limit before resolving this level. Some of the spectra contain additional small peaks that may be attributed to excited longitudinal states, having nodes along the QR axis, or to charging effects (see below). The lowest curve presents a spectrum taken on a rod having dimensions of 11×7 nm, thus the length is comparable to the Bohr radius. Consequently, quantum confinement effects related to the longitudinal dimension start becoming significant, thus enlarging the energy gap.

The VB is considerably more dense and complex and its level structure was not reliably resolved in our tunneling spectra; thus we only denote the first (ground state) peak as VB1 (see Fig. 7). Further insight regarding the QR level structure, including the excited VB levels, is gained by correlating the tunneling spectra with allowed optical VB to CB transitions, and both measurements with theoretical calculations.

In Fig. 8 we present a tunneling spectrum of a single QR in the QR\DT\Au configuration. As shown previously for QDs,¹³ the DT layer may promote single-electron charging due to the reduction in the QR-to-substrate tunneling rate. Indeed, the main difference from the spectra presented in Fig. 7 is the appearance of peak-multiplets attributed to single-electron charging multiplets, which may reflect the degeneracy of the corresponding levels.^{2,3,32} At positive bias, right above

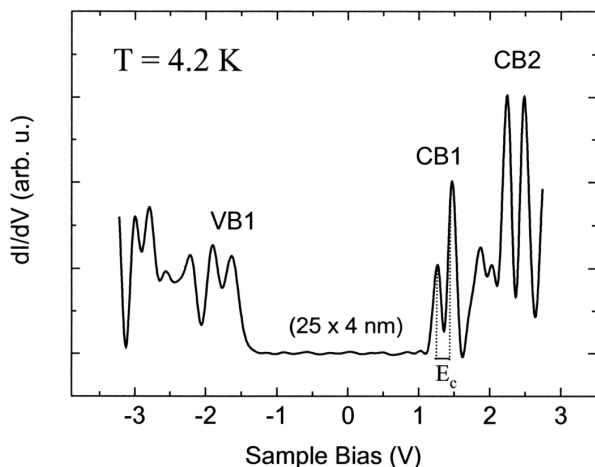


Fig. 8. dI/dV versus V tunneling spectra of a CdSe QR anchored to gold (QR\DT\Au configuration) having 4 nm diameter and 25 nm length. The main groups of peaks are defined by CB1, CB2, and VB1. Each state contains at least two peaks, attributed to single-electron charging multiplets. The apparent charging energy, enlarged due to voltage division in the DBTJ, is marked as E_c .

the energy gap, a doublet is clearly observed, signifying that the conduction-band ground state, CB1, is doubly (spin) degenerate, as expected for a particle in a cylindrical box (see model below). The inter-doublet spacing corresponds, up to voltage division enlargement,¹⁴ to the single-electron charging energy. The spectra at higher positive bias (above 2 V) are more complicated and hard to interpret, as will be further discussed below. In short, the two first smaller peaks are attributed to tunneling through the CB2 states while the CB1 level remains unoccupied (un-charged). The next two peaks correspond to the condition where the CB1 level is occupied, and the CB2 levels become charged. However, intrinsic (onset of field emission) and experimental (saturation of the pre-amplifier) limits of the available voltage range in the tunneling spectra, did not allow us to fully resolve the CB2 level degeneracy (which appears to be higher than two). InAs QRs, having a narrower band gap,⁹ are promising candidates for investigating the degeneracy of the excited energy states. In this system one may expect to observe more peaks in the available bias range.

MODEL

To accompany the experimental results and to assist in their interpretation, we used an effective-mass approximation approach in order to calculate the electronic structure of the QRs, following the formalism devel-

oped by Sercel and Vahala for quantum wires.³³ The same basis functions as in ref 33 were employed, using the following notation for the quantum numbers: n , the principal number, and F_z and L_z , the projections of the total and envelope angular momenta along the z axis, respectively. Here $F_z = J_z + L_z$ where J is the zone center Bloch angular momentum of the bulk bands. The finite length of the rods brings about an additional quantum number denoted by m (associated with the number of nodes along the QR axis, $m - 1$), replacing the continuous wave vector k_z in ref 33, and accordingly the eigenfunction is multiplied by a factor $\exp(imz)$.

The conduction-band states are calculated by using the uncoupled single-band model for a particle in a finite ($U = 5$ eV) cylindrical potential-well. Figure 9 presents the first three CB energy levels with $m = 1$, denoted as CB1, CB2, and CB3. We note here that according to this model, and for the $m = 1$ states, CB1 ($L_z = 0$) is twofold (spin) degenerate, while higher CB states ($|L_z| > 0$) are fourfold degenerate, as L_z can accept positive and negative values. It is evident also from the model that the energy levels depend strongly on the rod radius (Fig. 9a), with a much weaker dependence on length (Fig. 9b) in the region studied here. This is due to the strong confinement in the small (radial) direction. Indeed, short rods, with length approaching the bulk Bohr radius, or higher m states, effectively shortening the rods, do show significant length dependence.

The VB states have been calculated using a four-band effective-mass $\mathbf{k}\cdot\mathbf{p}$ model,³³ which couples the heavy and light holes, in an infinite potential-well for $F_z = 1/2, 3/2, 5/2$. Calculated VB levels are described in ref 12, where they were divided into three groups of closely spaced (effectively degenerate) states denoted as VB1, VB2, and VB3. We note that each of these levels, and in fact each F_z level, contains contributions of various L_z components, resulting in weak selection rules for optical transitions, thus complicating the assignment of the optical spectra.

DISCUSSION

a. Quantum Rod Level Structure

In Fig. 10 we compare the measured optical transitions and tunneling spectra with our theoretical calculations. The gap extracted from the optical measurements (solid circles) and the gap identified in the tunneling data (empty squares), are plotted along with the calculated energy gap, VB1–CB1.

In order to compare with the quasi-particle (tunneling) gap, the measured excitonic (optical) gap was corrected for the electron-hole Coulomb interaction. As a first approximation, we modified the expression given

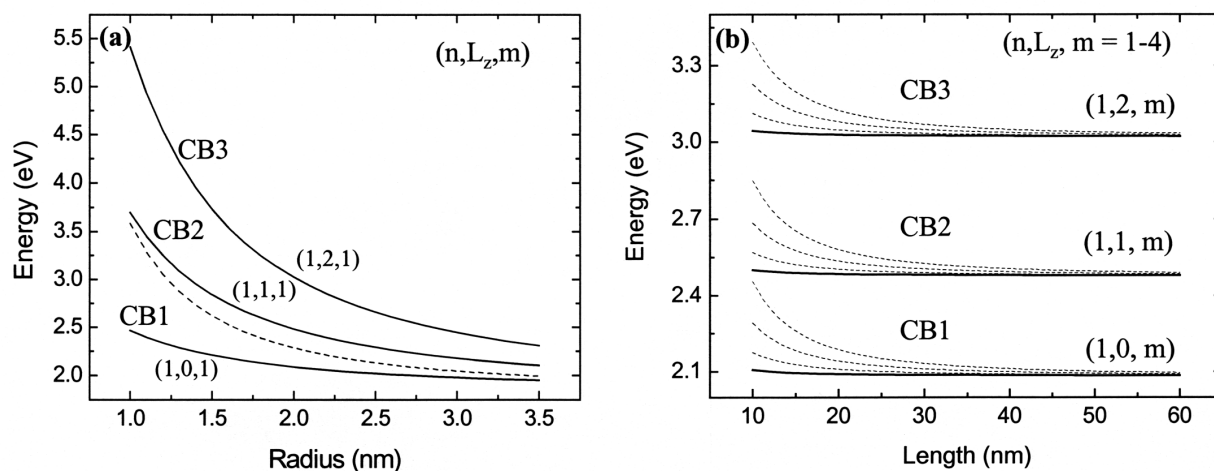


Fig. 9. Conduction band energy levels of CdSe QRs calculated for a confining potential of 5 eV. (a) First three energy states with $m = 1$ versus QR radius, for a 30 nm long QR. The quantum numbers (n, L_z, m) are denoted. The dashed line presents the position of the ground state as calculated using an infinite potential-well as in ref 12. (b) Length dependence for the respective energy levels for a rod 2 nm in radius, showing also the dependence on the quantum number m , for $m = 1$ (solid lines) and $m = 2-4$ (dashed lines). The energies are given with respect to the bulk VB edge.

in ref 34 for QDs, $1.8 e^2/k_r$ (where k is the dielectric constant), to take into account the fact that strong confinement holds primarily for the radial dimension of the QRs. We thus replace the radius, r , by $(r^2 a_0)^{1/3}$ where a_0 is the bulk CdSe Bohr radius, 5.7 nm. A relatively good agreement between the calculated and measured energy

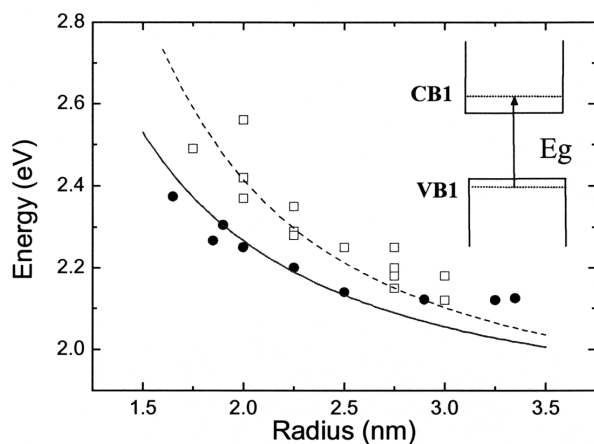


Fig. 10. Energy gap versus QR radius. The tunneling data (empty squares, size digitized due to radii uncertainty) and the model (solid and dashed lines represent finite and infinite potential-wells, respectively) correspond to the energy separations VB1–CB1. The optical data (solid circles) were determined from the first absorption peak and corrected for the electron-hole Coulomb interaction, see text. Inset: An illustration of the band-gap optical transition from VB1 to CB1.

gaps is found for both tunneling and optical experiments. However, the tunneling gaps are higher in energy, as was previously observed for QDs.² This can be ascribed to the effect of voltage division in the DBTJ, namely, to the non-vanishing voltage drop on the QR–substrate junction, enlarging the measured level spacing,^{13,18,19} and to the overestimated QR radii measured by STM due to convolution with the tip.²

Turning now to the excited levels, Fig. 11 shows spacings of the PLE transitions with respect to the band-gap transition, along with levels CB2 and CB3 measured with respect to CB1, detected by tunneling. The data are presented as a function of the band gap measured in each experiment, thus eliminating the possible problem of QR radius estimation mentioned above. PLE transition I (relative to E_g , solid circles) correlates well with the calculated level separation between VB1 and VB2, enabling one to assign it to the transition from VB2 to the CB ground state, CB1 (see Fig. 11b).

The assignment of PLE transition II is not as straightforward. In the lower energy-gap (thick rods) regime, $E_g < 2.12$ eV (solid down-pointing triangles), as well as in the regime of $E_g > 2.25$ eV (solid diamonds), this transition corresponds fairly well with the calculated level separation CB2–CB1. Therefore, it appears that PLE transition II takes place from the VB ground state (VB1) to CB2. This interpretation gains further support from the relatively good correlation with the CB2–CB1 level separation extracted from the tunneling experiment (empty squares) in the regime where the corresponding

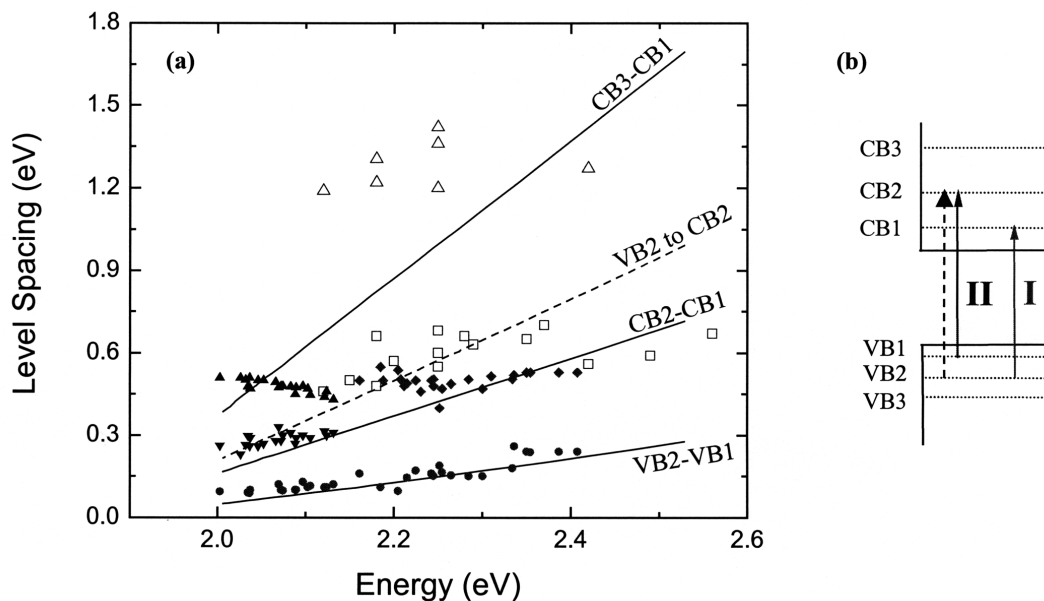


Fig. 11. (a) Excited energy states versus energy gap. The respective separations between the tunneling peaks are denoted by open symbols: CB2–CB1 (squares), CB3–CB1 (triangles). Spacing between the PLE transitions and the optical energy gap are presented by solid symbols: PLE I (circles), PLE II (down-pointing triangles and diamonds), PLE III (up-pointing triangles). The calculated energy level separations are depicted by the lines and marked. VB2 to CB2 corresponds to $|CB2-CB1|+|VB2-VB1|$. For the optical data, the energy gap was taken as the detection window corrected for the Coulomb interaction. The STM data represent 15 (out of 20) QRs whose spectra showed clear charging-free peak structure. (b) An illustration of the relevant excited optical transition from different VB states to CB states.

band gaps overlap (considering, again, the voltage division-induced enlargement in the tunneling experiments). However, at the intermediate band-gap regime, the experimental data for PLE transition II appear to merge with those of PLE transition III (solid up-pointing triangles), which was observed only for thick (low band-gap) QRs, complicating the assignment of PLE II. In fact, in this region also the calculated VB2 to CB2 transition (shown in dashed line and dashed arrow) seems to correspond better with the PLE data.

In this intermediate regime there may be an avoided crossing behavior, which is not completely resolved in our data. The difficulty in resolving this phenomenon and the PLE assignment in general, arises from the broad PLE peaks (about 200 meV) that appear in our spectra, under which several transitions could overlap. Note also that the second peak (transition II) observed in the PLE spectra of large energy-gap QRs (curves a–c in Fig. 4), has a non-Lorentzian line shape, suggesting that more than one transition contributes to this peak. In this respect it is important to recall that in our discussion of the model we grouped close-lying VB states, which cannot be resolved in our experiments, into single representative states.¹²

Compared with QDs, the experimental PLE peaks for rods are significantly broader, and therefore it is much more difficult to provide unambiguous level assignment. The tunneling spectra, especially for the VB states, are also significantly less structured compared to dots. This behavior for both PLE and tunneling matches the theoretical model that exhibits a complex and dense VB level structure. Additionally, the spectral lines in both experiments are further broadened due to the contribution of excited *m*-levels. This reflects the significant increase in the density of states for rods compared with dots, as part of the manifestation of the transition from a zero-dimensional to a quasi one-dimensional system.

b. Single-Electron Charging Effects

Figure 12 presents tunneling spectra measured on two QRs similar in size (25 nm long and 4 nm in diameter) for the two different tunneling configurations described above. The (a) spectrum in Fig. 12 was acquired on a QR deposited directly on HOPG, while that in (b) was obtained for the QR/DT/Au configuration. It is evident that single-electron charging effects are significant in spectrum (b), whereas they are suppressed in

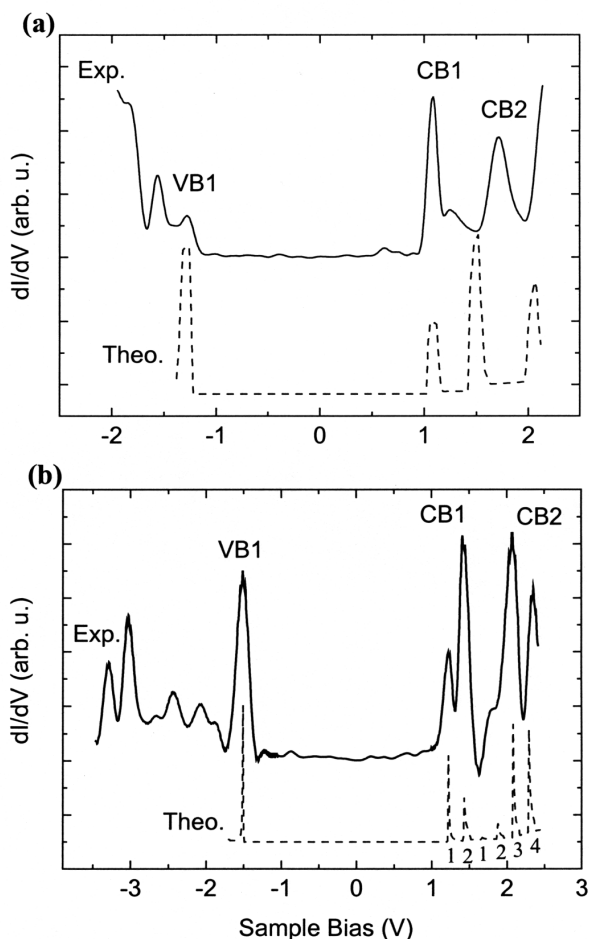


Fig. 12. dI/dV versus V tunneling spectra (solid lines) of two similar CdSe QRs (4×25 nm), one deposited on HOPG (a) and the other attached to gold via DT molecules (b). The dashed lines represent simulations calculated using the theory for single-electron tunneling, shifted vertically for clarity. In both cases we used the same values for the band gap and CB2–CB1 level spacing, $E_g = 2.20$ eV and $\Delta_{CB} = 0.39$ eV (the more complex VB was not simulated). The fits differ only in the tunneling junction parameters. The capacitance values are $C_1 = 1 \times 10^{-19}$ F and $C_2 = 50 \times 10^{-19}$ F in frame (a), while $C_1 = 1.1 \times 10^{-19}$ F and $C_2 = 7.7 \times 10^{-19}$ F for frame (b). The ratio between the tunneling rates between the two junctions is $\Gamma_2/\Gamma_1 = 10$ in frame (a), suppressing charging effects, whereas $\Gamma_2/\Gamma_1 = 0.2$ in (b), enhancing QR charging. The numbers below the fit in (b) denote the charging state of the QR.

(a) (note the small peak to the right of CB1 that may be a hint of a charging phenomenon). This is due, as mentioned above, to the reduced tunneling rate $\Gamma \sim 1/R$ in junction 2 resulting from the presence of the DT layer. The simulated spectra, presented in dashed lines in Fig. 12 and described below, support this interpretation,

and corroborate our discussion of Fig. 8 concerning the charging effects.

The spectra were simulated using the theory for single-electron tunneling in a DBTJ configuration,³⁵ modified to treat nanoparticles having a discrete level spectrum.^{14,32} Since the QRs in both cases were very similar in size, we used the same values for the band gap and CB2–CB1 level spacing, $E_g = 2.20$ eV and $\Delta_{CB} = 0.39$ eV (which correspond well with our energy level calculations). The fits differ only in the tunneling junction parameters. The capacitance values are $C_1 = 1 \times 10^{-19}$ F and $C_2 = 50 \times 10^{-19}$ F for spectrum (a), while $C_1 = 1.1 \times 10^{-19}$ F and $C_2 = 7.7 \times 10^{-19}$ F in (b). The decrease in C_2 for case (b) may reflect the increase of QR–substrate distance due to the DT layer and possibly to a change in the effective dielectric function. The important difference between these two pairs of parameters is the ratio, C_1/C_2 , which is much larger in (b). This ratio determines the voltage division between the two junctions, $V_1/V_2 = C_2/C_1$, and consequently the ratio between measured to real level spacing, $1 + C_1/C_2$. In spectrum (b) this enlargement effect is significant, resulting, e.g., in an apparently large energy gap (note the difference in the bias scales between the two frames). The typical charging energy found in our experiment (inter-multiplet peak separation, see Fig. 8) was about 180 meV, after correcting for the voltage division effect, comparable to our previous observation for InAs QDs.²

More pronounced is the effect of the tunneling rates ratio between the two junctions. In the QR\HOPG case it is $\Gamma_2/\Gamma_1 = 10$, suppressing charging effects, whereas $\Gamma_2/\Gamma_1 = 0.2$ for the QR\DT\Au configuration, enhancing QR charging. The numbers below the fit in the latter case (Fig. 12b) denote the number of excess electrons on the QR. The simulation shows that tunneling through the CB2 levels may take place without charging the CB1 level. The probability for that is small for the parameters used in the simulation, resulting in two small peaks in the simulated spectra. The shoulder at the lower bias side of the CB2 peak in the corresponding experimental spectrum (and the two small peaks at the lower bias side of the CB2 levels in Fig. 8) are attributed to that scenario. Note also that here too, as discussed for Fig. 8, the degeneracy of the CB2 level could not be determined.

CONCLUSIONS

Combined optical and tunneling spectroscopy measurements provide a powerful tool for investigating the level structure of semiconductor QRs. The experimental data obtained for CdSe QRs, from both optical and tunneling measurements, show that the level structure is dominated by radius rather than by length, and they correspond to model calculations with reasonable agreement.

This behavior depicts the quasi one-dimensional nature of the QRs even for aspect ratios as small as three and lengths above ~ 10 nm. This can be qualitatively understood by considering the dimensions of CdSe QRs compared with the bulk exciton Bohr radius. For rods longer than 10 nm, the weak confinement regime is already approached for the long dimension (the axis), while strong confinement still persists for the lateral dimension in the diameter regime studied.

These electronic properties allow one to select a desired QR length and tune its optical or electrical properties at will, using the diameter. This ability is of significant importance for future nanotechnology applications of QRs.^{5,36} The single-electron charging multiplets measured on these nanocrystals clearly revealed the degeneracy of the CB ground state, but further investigations on QRs made of narrow band-gap semiconductors are still needed in order to reveal the degeneracy of excited states.

Acknowledgments. This work was supported in part by grants from the United States-Israel Binational Science Foundation, the DIP (Deutsche Israel Program), the Israel Ministry of Science, and the Israel Science Foundation.

REFERENCES AND NOTES

- Alivisatos, A.P. *Science* **1996**, *271*, 933.
- Banin, U.; Cao, Y.W.; Katz, D.; Millo, O. *Nature* (London) **1999**, *400*, 542.
- Millo, O.; Katz, D.; Cao, Y.W.; Banin, U. *Phys. Rev. Lett.* **2001**, *86*, 5751.
- Klimov, V.; Mikhailovsky, A.; Xu, S.; Malko, A.; Hollingsworth, J.A.; Leatherdale, C.A.; Eisler, H.J.; Bawendi, M.G. *Science* **2000**, *290*, 314.
- Kazes, M.; Lewis, D.Y.; Ebenstein, Y.; Mokari, T.; Banin, U. *Adv. Mater.* **2002**, *14*, 317.
- Tessler, N.; Medvedev, V.; Kazes, M.; Kan, S.H.; Banin, U. *Science* **2002**, *295*, 1506.
- Bruchez, M.; Moronne, M.; Gin, P.; Weiss, S.; Alivisatos, A.P. *Science* **1998**, *281*, 2013.
- Peng, X.G.; Manna, L.; Yang, W.D.; Wickham, J.; Scher, E.; Kadavanich, A.; Alivisatos, A.P. *Nature* (London) **2000**, *404*, 59.
- Kan, S.H.; Mokari, T.; Rothenberg, E.; Banin, U. *Nat. Mater.* **2003**, *2*, 155.
- Hu, J.T.; Li, L.S.; Yang, W.D.; Manna, L.; Wang, L.W.; Alivisatos, A.P. *Science* **2001**, *292*, 2060.
- Chen, X.; Nazzari, A.; Goorskey, D.; Xiao, M.; Peng, Z.A.; Peng, X. *Phys. Rev. B* **2001**, *64*, 5304.
- Katz, D.; Wizansky, T.; Millo, O.; Rothenberg, E.; Mokari, T.; Banin, U. *Phys. Rev. Lett.* **2002**, *89*, 86801; Erratum, **2002**, *89*, 199901.
- Katz, D.; Millo, O.; Kan, S.H.; Banin, U. *Appl. Phys. Lett.* **2001**, *79*, 117.
- Millo, O.; Banin, U. *Annu. Rev. Phys. Chem.* **2003**, *54*, 465.
- Norris, D.J.; Bawendi, M.G. *Phys. Rev. B* **1996**, *53*, 16338.
- Banin, U.; Lee, C.J.; Guzelian, A.A.; Kadavanich, A.V.; Alivisatos, A.P.; Jaskolski, W.; Bryant, G.W.; Efros, A.L.; Rosen, M. *J. Chem. Phys.* **1998**, *109*, 2306.
- Chen, S.; Ingram, R.S.; Hostetler, M.J.; Pietron, J.J.; Murray, R.W.; Schaaff, T.G.; Khoury, J.T.; Alvarez, M.M.; Whetten, R.L. *Science* **1998**, *280*, 2098.
- Bakkers, E.P.A.M.; Vanmaekelbergh, D. *Phys. Rev. B* **2000**, *62*, R7743.
- Bakkers, E.P.A.M.; Hens, Z.; Zunger, A.; Franceschetti, A.; Kouwenhoven, L.P.; Gurevich, L.; Vanmaekelbergh, D. *Nano Lett.* **2001**, *1*, 551.
- Franceschetti, A.; Zunger, A. *Phys. Rev. B* **2000**, *62*, 2614.
- Lee, S.; Kim, J.; Jönsson, L.; Wilkins, J.W.; Bryant, G.W.; Klimeck, G. *Phys. Rev. B* **2002**, *66*, 235307.
- Niquet, Y.M.; Delerue, C.; Allan, G.; Lannoo, M. *Phys. Rev. B* **2002**, *65*, 165334.
- Ekimov, A.I.; Hache, F.; Schanneklein, M.C.; Ricard, D.; Flytzanis, C.; Kudryavtsev, I.A.; Yazeva, T.V.; Rodina, A.V.; Efros, A.L. *J. Opt. Soc. Am. B* **1993**, *10*, 100.
- Li, X.Z.; Xia, J.B. *Phys. Rev. B* **2002**, *66*, 115316.
- Hu, J.T.; Wang, L.W.; Li, L.S.; Yang, W.; Alivisatos, A.P. *J. Phys. Chem.* **2002**, *106*, 2447.
- Li, J.; Wang, L.W. *Nano Lett.* **2002**, *3*, 101.
- Manna, L.; Scher, E.C.; Alivisatos, A.P. *J. Am. Chem. Soc.* **2000**, *122*, 12700.
- Peng, Z.A.; Peng, X. *J. Am. Chem. Soc.* **2001**, *123*, 1389.
- Mokari, T.; Banin, U. *Chem. Mater.* **2003**, *15*, 3955.
- Tews, M.; Pfannkuche, D. *Phys. Rev. B* **2002**, *65*, 073307.
- Li, L.S.; Hu, J.T.; Yang, W.D.; Alivisatos, A.P. *Nano Lett.* **2001**, *1*, 349.
- Millo, O.; Katz, D.; Cao, Y.W.; Banin, U. *Phys. Rev. B* **2000**, *61*, 16773.
- Sercel, P.C.; Vahala, K.J. *Phys. Rev. B* **1990**, *42*, 3690.
- Brus, L.E. *J. Chem. Phys.* **1984**, *9*, 4403.
- Hanna, A.E.; Tinkham, M. *Phys. Rev. B* **1991**, *44*, R5919.
- Huynh, W.U.; Dittmer, J.J.; Alivisatos, A.P. *Science* **2002**, *295*, 2425.

Copyright of Israel Journal of Chemistry is the property of Laser Pages Publishing Ltd. and its content may not be copied or emailed to multiple sites or posted to a listserv without the copyright holder's express written permission. However, users may print, download, or email articles for individual use.